Evidence of 3D Topological-Domain Dynamics in KTN:Li Polarization-Supercrystal Formation

Feifei Xin,[1,2,*] Ludovica Falsi,[1] Yehonatan Gelkop,[3] Davide Pierangeli,[1,4] Guoquan Zhang,[2] Fang Bo,[2] Fabrizio Fusella,[1] Aharon J. Agranat,[3] and Eugenio DelRe[1,5]

[1]*Dipartimento di Fisica, Università di Roma "La Sapienza", 00185 Rome, Italy*
[2]*The MOE Key Laboratory of Weak-Light Nonlinear Photonics, School of Physics and TEDA Applied Physics Institute, Nankai University, Tianjin 300071, China*
[3]*The Institute of Applied Physics, The Hebrew University, Jerusalem 91904, Israel*
[4]*Institute for Complex Systems, National Research Council, Rome 00185, Italy*
[5]*ISC-CNR, Università di Roma "La Sapienza", 00185 Rome, Italy*

(Received 7 April 2023; revised 31 October 2023; accepted 5 January 2024; published 9 February 2024)

We experimentally and theoretically investigate thermal domain evolution in near-transition KTN:Li. Results allow us to establish how polarization supercrystals form, a hidden 3D topological phase composed of hypervortex defects. These are the result of six converging polarization vortices, each associated to one orientation of the 3D broken inversion symmetry. We also identify rescaling soliton lattices and domain patterns that replicate on different scales. Findings shed light on volume domain self-organization into closed-flux patterns and open up new scenarios for topologically protected noise-resistant ferroelectric memory bits.

DOI: 10.1103/PhysRevLett.132.066603

Closed-flux topological domain patterns in ferroelectric and ferromagnetic materials are key in exploring new states of matter and in designing robust information and energy storage devices [1–6]. Noise-resistant bits can be realized using polarization vortices, topologically protected defects in which the spontaneous polarization wraps around in a plane [7]. Ideally, 3D defects, i.e., localized closed-flux patterns where polarization wraps around in a volume, will have an intrinsically stronger topological protection, thus potentially increasing storage density [5,8–12]. High-dimensional topological defects are known to form spontaneously in liquid-crystals, nanomagnets, and layered systems, where both ferromagnetic and ferroelectric skyrmions have been reported [13–21]. Ferroelectric perovskites cooled to their Curie temperature T_C also manifest 3D polar domain patterns [22]. In bulk samples of compositionally disordered KTN:Li and KTN:Cu, the patterns extend periodically throughout the sample to become so-called ferroelectric polarization supercrystals (SCs) [23–29]. SCs enucleate in transparent samples from built-in striations to have a micrometric lattice constant Λ typical of photonic crystals. Striations are a commonly observed consequence of segregation in the growth of bulk crystals [30,31], a patterning of composition that, in ferroelectrics, causes an equally patterned T_C [32,33]. These polarization SCs form a unique photonic material, a lattice of interlocked 3D-rotated birefringent elements [23–27] with striking optical properties, such as giant broadband refraction [34–36]. In terms of spontaneous polarization, the ferroelectric order-parameter, SCs are thought to be a superlattice of hypervortices (HVs), a network of 3D topological defects that agrees with available experimental results and achieves the screening of polarization charge and elastic stress [23,24]. Each HV lattice cell consists of 6 vortex structures interlocked together to form an overall mesoscopic cubelike building block. In many aspects, HVs appear as a 3D generalization of the spontaneous polarization closed-flux vortex domain patterns originally discussed by Landau, Lifshitz, and Kittel for ferromagnetic systems [37–40]. While recent studies corroborate the existence of stable ferroelectric 3D patterns [5,41], the mechanism that leads to the spontaneous formation of an SC is presently unclear.

We here analyze the thermal evolution of ferroelectric domain patterns and SC formation in near-transition KTN:Li using stereoscopic far-field and direct-field laser transmission microscopy and phase-field simulations based on the Ginzburg-Landau theory. This allows us to determine the physical underpinnings of the SC. A stable SC emerges as a hidden topological phase, a history-dependent state where HVs form extended and coherent networks as the sample is first cooled and then heated at the phase transition. Monotonically cooling from the paraelectric phase leads to an SC characterized by a spatially shifting and rescaling lattice of polarization solitons, while a strongly temperature-dependent multiscale-SC domain pattern appears as the sample is heated or cooled from the temperature region where history dependence is observed.

Experiments are performed in a bulk 2.5 mm (x) by 2.0 mm (y) by 1.9 mm (z) $K_{0.997}Ta_{0.64}Nb_{0.36}O_3:Li_{0.003}$

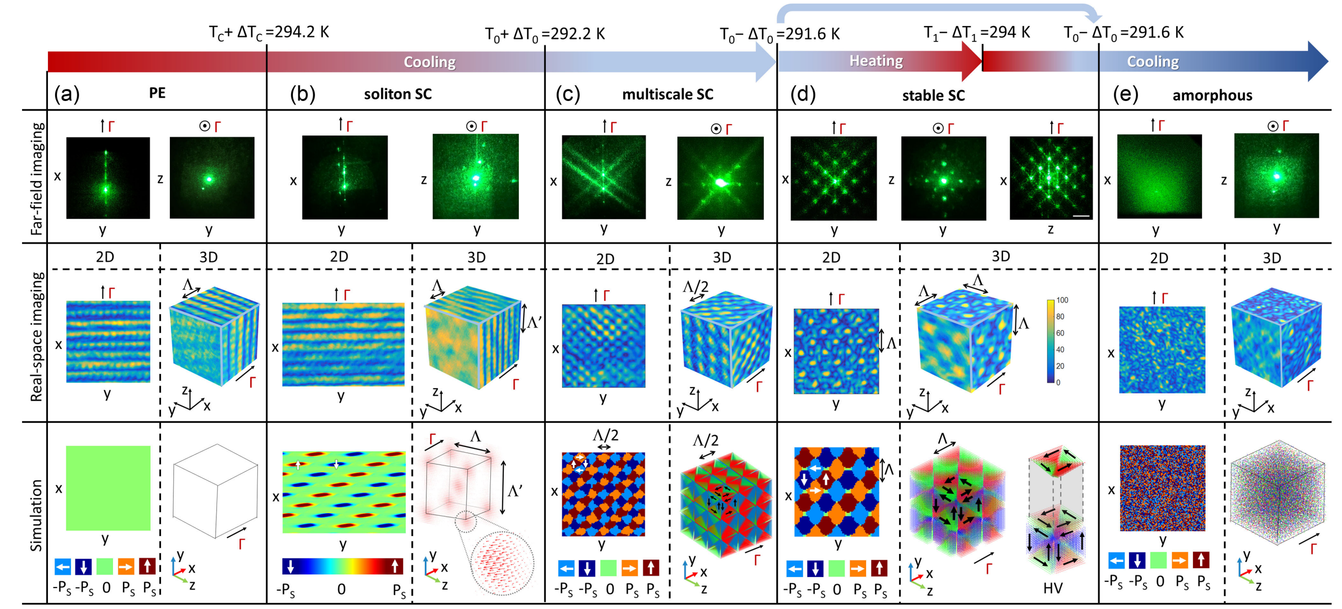

FIG. 1. Temperature-driven domain patterns during the cooling-heating process for the (a) PE phase, (b) soliton-SC state, (c) multiscale-SC state, (d) stable-SC state, and (e) amorphous state. First row: far-field imaging. Scale bar is 4° (xz distributions are found to be analogous to the xy distributions and are reported only for the stable SC). Second row: real-space imaging. Λ is the lattice constant of the stable SC. Λ' is the lattice constant of the soliton SC along y and z. Third row: simulation of the $\mathbf{P}$ distribution. For the 3D model, red (for $\pm\mathbf{u}_x$), blue (for $\pm\mathbf{u}_y$), and green (for $\pm\mathbf{u}_z$) arrows illustrate the resulting 3D $\mathbf{P}$ field of the meshed grids in simulation. Black arrows indicate the average $\mathbf{P}$ orientation in a single domain.

(KTN:Li) perovskite. The sample undergoes a transition from a cubic m$\bar{3}$m-symmetry paraelectric (PE) phase to a tetragonal 4mm-symmetry ferroelectric (FE) phase, characterized by a temperature region $T_0 < T < T_1$ ($T_0 \simeq 291.9$ K, $T_1 \simeq 294.3$ K, $T_C \simeq 293.9$ K), where history dependence (HE) is observed [28,29]. The appearance of an HE temperature region is common to a wide class of disordered ferroelectrics with a dipolar glasslike response [42–44]. A key feature is that the sample has a striation pattern, i.e., a periodic change in composition along the growth direction (x) of period $\Lambda/2$: this causes a periodic distribution of $T_0(x)$, $T_C(x)$, and $T_1(x)$ [i.e., $T_j(x) = T_j - \Delta T_j \sin[2\pi x/(\Lambda/2)]$, with $j = 0, C, 1$] [33,45,46]. Spontaneous polarization $\mathbf{P}$ forms along one of the cubic principal axes, leading to birefringent polar domain patterns that can be analyzed using direct-field and far-field laser transmission microscopy. The formation and thermal dynamics of the domains are theoretically analyzed using phase-field simulations, a numerical approach to the Ginzburg-Landau theory and Maxwell's macroscopic equations, here specialized to KTN:Li, that allows us to predict the $\mathbf{P}$ field [41,47]. Details on the setup, material, and numerical simulations are described in the Supplemental Material Secs. I and II [48].

Temperature-driven domain pattern phenomenology observed by far-field and direct-field laser transmission microscopy are reported in the first row and second row of Fig. 1, respectively. Simulations of the $\mathbf{P}$ field are shown in the third row. Images are taken in the directions of z (xy plane), x (yz plane), and y (xz plane), parallel to the three cubic lattice axes of the zero-cut sample. Relevant simulations of 2D images [i.e., where space coordinates are $\mathbf{r} = (x, y)$ and $\mathbf{P} = (P_x, P_y)$, left column of each panel] and full 3D models (right column of each panel) are compared with the real-space 2D images and 3D combined images. For $T > 294.2$ K, deep in the PE phase [Fig. 1(a)], a characteristic striation pattern is revealed by the far-field and real-space imaging. A discrete spatial spectrum for light propagating perpendicular to the growth direction Γ is evident in the far field, and absent for light transmitted along Γ. Real-space images show a periodic planar index of refraction distribution of period $\Lambda/2 = 7.5$ μm. The simulated PE phase has consistently $\mathbf{P} = 0$.

As reported in Fig. 1(b), cooling below $T_C + \Delta T_C$, into the HE region, real-space imaging shows a volume periodic domain pattern, with a $\Lambda = 15$ μm along Γ, and $\Lambda' \simeq 20$ μm in the other two directions. The pattern appears to translate rigidly as a soliton SC in a direction normal to Γ along the yz diagonal, until T is further decreased down to $T_0 + \Delta T_0$. Simulation shows that, cooling from the PE phase, a range of temperatures $T_C + \Delta T_C < T < T_0 + \Delta T_0$ is able to support solitons, i.e., localized regions of finite $\mathbf{P} \neq 0$ embedded in an otherwise subcooled PE background, for which diffusion is compensated by nonlinearity [49,50] (see Supplemental Material, Sec. II [48]). These solitons can be arranged into close-packed geometries, fixed by the striation pattern Λ along Γ, to reproduce the observed results reported in Fig. 1(b) second

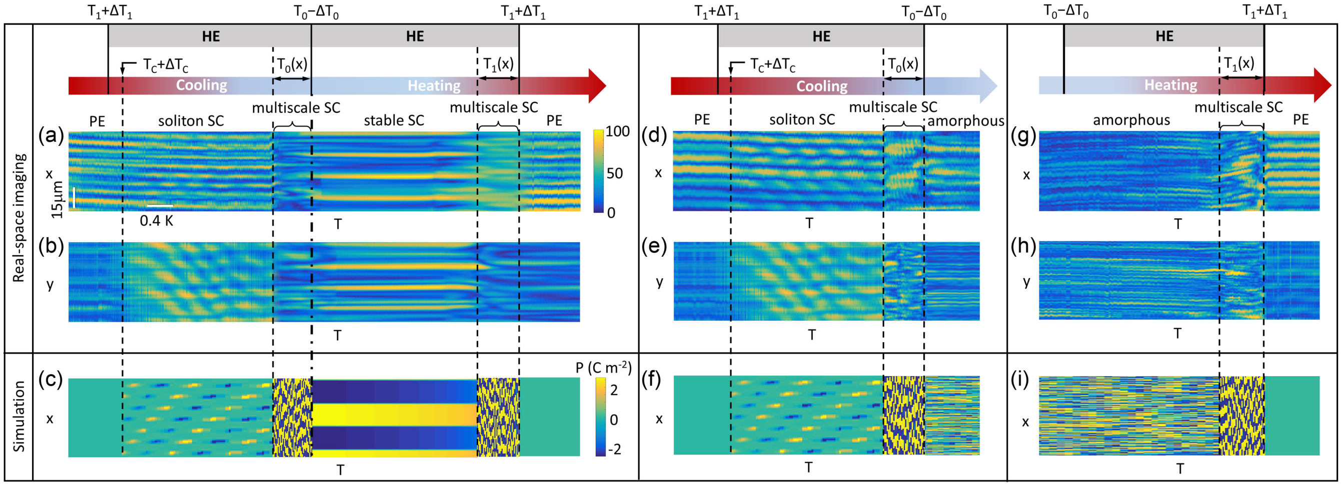

FIG. 2. Temperature dynamics and history dependence. States versus T for cooling and reheating at $T_0 - \Delta T_0$, resulting in the appearance of stable SC, for the (a) growth axis (x axis) versus T, (b) y axis versus T real-space imaging, and (c) x axis versus T simulation. Monotonic cooling from $T > T_1 + \Delta T_1$ to $T < T_0 - \Delta T_0$ for (d) x axis versus T, (e) y axis versus T real-space imaging, and (f) x axis versus T simulation. Monotonic heating from $T < T_0 - \Delta T_0$ to $T > T_1 + \Delta T_1$ for (g) x axis versus T, (h) y axis versus T real-space imaging, and (i) x axis versus T simulation.

row. The scale Λ' is T dependent: this causes the entire soliton lattice to translate along the yz diagonal as found in experiments (see Fig. 2).

At $T_0 + \Delta T_0 = 292.2$ K, the far-field begins to manifest continuous diagonal lines, suggesting a highly anisotropic continuum of scales typical of a multiscale SC [Fig. 1(c), first row]. In real space, the pattern undergoes a rapid series of changes, a sample of which is shown in Fig. 1(c), second row. For the achievable resolution of the stereoscopic laser transmission scheme, images appear to show different patterns in the zy plane, xy plane, and xz planes, and a rescaled $\Lambda/2 \simeq 7.5$ μm lattice constant. Higher resolution phase-contrast microscopy shown in Fig. S4 in Supplemental Material unveils a multiscale-SC domain pattern [48]. Cooling below $T_0 + \Delta T_0$, simulations lead to phenomenology in which the PE regions are superseded by polar regions. In agreement with experiments, a multiscale-SC state appears. Figure 1(c) third row displays solutions with the same period $\Lambda/2$ in the x and y and in the x, y, and z directions for the 2D and 3D cases, respectively. Here the SC patterns change scales with temperature in the range $T_0 + \Delta T_0 > T > T_0 - \Delta T_0$, manifesting a transient behavior similar to observations. In two dimensions, the rescaling structure is a vortex lattice, while in three dimensions, a signature rescaling lattice of HVs is found (the 3D multiscale SC). As illustrated in Fig. 1(d) bottom right, each cell of the superlattice is formed by six pyramidlike vortices locked together into a cubelike assembly. Further cooling through $T_0 - \Delta T_0 = 291.6$ K causes the far field to turn into a continuous spectrum in all directions, typical of an amorphous state [Fig. 1(e)] that persists at lower T, in the FE region. In real space, the multiscale SC is superseded by a highly scattering optically amorphous state at $T_0 - \Delta T_0$, in agreement with the simulation results for $\mathbf{P}$ reported in Fig. 1(e) third row.

If we stop cooling at $T_0 - \Delta T_0$ and start reheating into the HE region, a thermally stable and spatially regular structured far-field and real-space distribution appears [Fig. 1(d)]. A sudden rearrangement of the domains leads to a stationary and stable SC pattern of lattice constant $\Lambda = 15$ μm for the entire range of $T_0 - \Delta T_0 < T < T_1 - \Delta T_1$ [the stability is demonstrated in Figs. 2(a) and 2(b)]. The pattern appears as a highly-symmetric body-centered-cubic (bcc) distribution in real space, corresponding to a periodic diffraction pattern in the far field. The SC dissolves either by heating the sample above $T_1 - \Delta T_1$, where the multiscale-SC and PE phase ensue [see Figs. 2(a) and 2(b)], or cooling it below $T_0 - \Delta T_0$, where the amorphous state of Fig. 1(e) appears and persists for lower T. As reported in Fig. 1(d) third row, the stable SC also appears in simulations: if on reaching $T_0 - \Delta T_0$ the system is reheated into the range $T_0 - \Delta T_0 < T < T_1 - \Delta T_1$, a stable, T-independent SC appears formed in 2D by a superlattice of vortices of period Λ, which in 3D emerges as a stable HV SC. In distinction to the multiscale SC, whose scale varies with T, here each HV is a fixed $\Lambda \times \Lambda \times \Lambda$ cube for all temperatures in the range, in agreement with the experiments.

Figure 2 reports the T evolution and history dependence of the states, with real-space images in good agreement with simulation results that demonstrate the underlying 4D nature of the process (4D = 3 spatial axes +1 temperature axis). In Figs. 2(a)–2(c) we report the experimental and numerical spatial profiles versus T for the cooling and reheating process. The average cooling and heating rate is 0.8 K/min. The transition from the PE to the soliton SC,

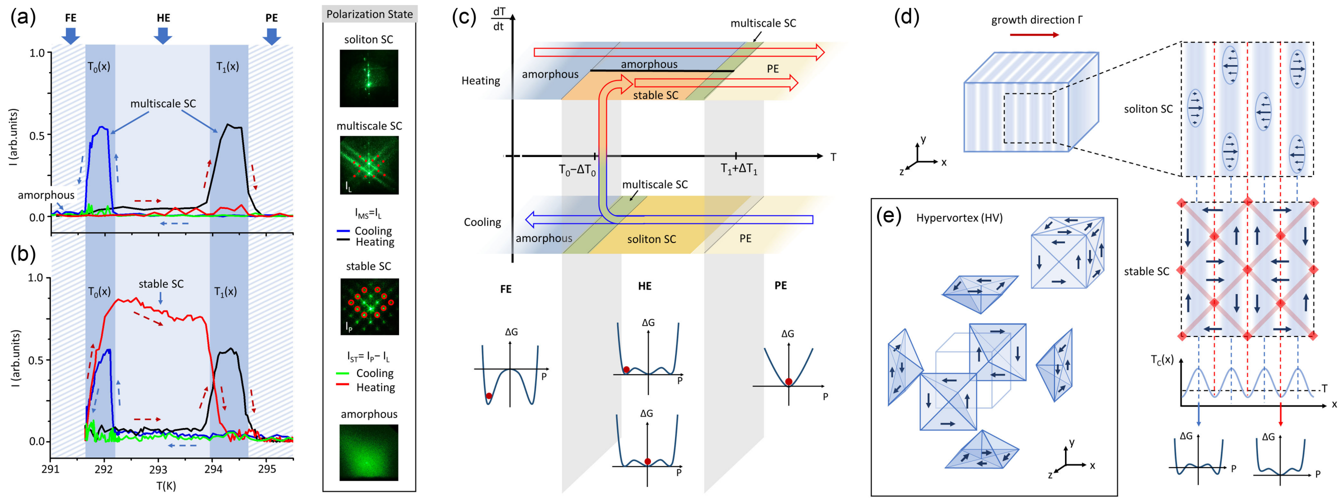

FIG. 3. Topological defect formation mechanism and stable SC as a hidden phase. (a) Monotonic cooling and heating with no stable SC, compared to (b) a cooling-reheating cycle in the HE region, with a strong stable-SC signal (red line). (inset) Dynamics are measured in terms of the multiscale-SC intensity I_{MS} for cooling (blue line) and heating (black line) and stable-SC intensity I_{ST} for cooling (green line) and heating (red line). (c) Phase diagram representation of the history-dependent thermal evolution. (d) Illustration of underlying P geometries and the role of striations in the formation and scaling of the soliton-SC and stable-SC states. (e) Illustration of an HV unit cell, six pyramidlike vortices locked together into a cube.

and multiscale SC during the cooling process is evident. Specifically, the soliton SC translates as T is decreased, manifesting a periodic pattern along the T axis with a period $\Lambda_T = 0.4$ K. Together with the periodic structure in all three spatial axes [Fig. 1(b)], the soliton SC has a characteristic 4D periodic lattice. Then a transient multiscale SC emerges until the crystal is reheated at $T_0 - \Delta T_0$, where a temperature-independent stable SC is found in the HE region. Figures 2(d)–2(f) show a monotonic cooling across the HE region, demonstrating transitions from the PE to the soliton SC, multiscale SC, and finally amorphous state (below $T_0 - \Delta T_0$). In Figs. 2(g)–2(i) we report the profiles for monotonic heating: an amorphous state occupies the HE region as it is heated from low temperatures ($T < T_0 - \Delta T_0$) to $T_1 - \Delta T_1$, where the sample manifests a multiscale SC for $T_1 - \Delta T_1 < T < T_1 + \Delta T_1$, and a PE state for $T > T_1 + \Delta T_1$. In distinction to the cooling results, here no soliton SC is observed. Furthermore, no stable SC is found in both the monotonic cooling and heating processes. The fact that three different states (soliton SC, stable SC, and amorphous) emerge in the HE region depending on the thermal history, is the signature of the HE region.

The hidden nature of the stable-SC phase can be further substantiated analyzing far-field temperature dynamics, as reported in Figs. 3(a) and 3(b). Introducing two parameters, the multiscale-SC intensity I_{MS} and the stable-SC intensity I_{ST} of the spatial spectrum (see inset in Fig. 3 and Sec. IV in the Supplemental Material [48]), the different cooling and heating behavior flags the HE region and the cooling and heating multiscale-SC peaks indicate the passage from the HE to the FE region and from the HE to the PE region, respectively. While monotonic cooling or heating leads to no phenomenology in the HE region [red and green line in Fig. 3(a)], cooling and reheating at $T \simeq T_0 - \Delta T_0$ into the HE region generates a strong stable-SC signal [red line in Fig. 3(b)].

Thermal dynamics are schematically illustrated in the phase diagram of Fig. 3(c). The T-dependent Gibbs free energy versus $\mathbf{P}$ curves underline how, in the HE region, both the inversion-symmetric $\mathbf{P} = 0$ and symmetry-breaking $|\mathbf{P}| = P_s$ states can act as ground states. SC formation and thermal evolution can then be discussed in terms of superlattices of topological defects, the natural result of spontaneous-symmetry breaking in a spatially extended system [51,52]. Each defect is a region where different domains, enucleated by parts of the system that have spontaneously relaxed into different ground states, meet and lock into a stalemate. As depicted in Fig. 3(d), the periodic striation pattern causes a spatially oscillating transition temperature $T_C(x)$, the seed for the formation and scaling of the SCs. Enucleation begins in the HE region in the crystal planes where $T_C(x)$ is maximum, and involves the appearance of close-packed solitons forming the soliton-SC state. On cooling, approaching $T_0 + \Delta T_0$ (the HE/FE boundary), the PE state in between the solitons disappears into a multiscale-SC state, and reheating at $T_0 - \Delta T_0$ back into HE causes the domain patterns to rearrange into the stable SC in the HE region. The topological defects emerge as domains arrange themselves, with electrically compatible "head-to-tail" polarization, into 2D Kittel-like vortices and 3D HVs. These are the result of either 2D or 3D combinations of the 90° and 180° degree domain walls that minimize energy. Simply cooling into the HE from the

PE region does not allow the defects to be seeded by the striations, as seeding must occur at the HE/FE boundary from the multiscale-SC distribution, while simply heating from the FE region causes the domains in the HE region to be those of the previous disordered amorphous state. Put differently, cooling and reheating serves the purpose of resetting the domain pattern and allowing it to be reprogrammed by the striations, leading to a stable lattice on reheating. The simulated HV unit cell in the bottom panel of Fig. 1(d), and a simplified model in Fig. 3(e) show how six different pyramidlike standard vortices are locked together forming an HV cube, a structure that confirms previous conjectures [23,24,35]. Singular topological defects at the center and saddle points of the HV form on the planes of the minima of $T_C(x)$, where the $\mathbf{P} = 0$ persists [see Fig. 3(d)].

In conclusion, we describe a detailed analysis of temperature-dependent ferroelectric spontaneous domain patterning using stereoscopic laser transmission imaging and phase-field simulations in near-transition KTN:Li. Results provide a physical understanding of ferroelectric supercrystal formation and evolution based on the enucleation and interaction of hypervortex topological defects. This allows us to establish the role of sample dimensionality, thermal history, and built-in striation patterns in forming a stable 3D topological phase, suggesting new ways to analyze and control, through temperature, the behavior of high-dimensional topological defects in other systems, such as materials supporting ferroelectric and ferromagnetic skyrmions [17,18,21].

We acknowledge support from the PNRR MUR Project No. PE0000023-NQSTI, PRIN 2020 MUR Project No. 2020X4T57A, PRIN 2022 MUR Project No. 20223T577Z, Sapienza-Ricerca di Ateneo Projects, H2020 Fet Project PhoQus, the Research and National Natural Science Foundation of China (Grant No. 12004282), and the Ministry of Innovation Science and Technology, Grants No. 88428 and No. 4698. This research was supported in part by the State of Israel Ministry of science technology and Space, Grant No. 4698.

*Corresponding author: cindy.feifeixin@gmail.com

[1] A. Vilenkin and E. P. S. Shallard, *Cosmic Strings and Other Topological Defects* (Cambridge University Press, Cambridge, England, 1994).
[2] Y. L. Tang, Y. L. Zhu, Z. L. Ma *et al.*, Observation of a periodic array of flux-closure quadrants in strained ferroelectric $PbTiO_3$ films, Science **348**, 547 (2015).
[3] J. M. Kosterlitz, Nobel lecture: Topological defects and phase transitions, Rev. Mod. Phys. **89**, 040501 (2017).
[4] T. Hirosawa, J. Klinovaja, D. Loss, and S. A. Díaz, Laser-Controlled Real- and Reciprocal-Space Topology in Multiferroic Insulators, Phys. Rev. Lett. **128**, 037201 (2022).
[5] C. Dai, V. A. Stoica, S. Das, Z. Hong, L. W. Martin, R. Ramesh, J. W. Freeland, H. Wen, V. Gopalan, and L. Chen, Tunable nanoscale evolution and topological phase transitions of a polar vortex supercrystal, Adv. Mater. **34**, 2106401 (2022).
[6] Y. Liu, K. P. Kelley, H. Funakubo, S. V. Kalinin, and M. Ziatdinov, Exploring physics of ferroelectric domain walls in real time: Deep learning enabled scanning probe microscopy, Adv. Sci. **9**, 2203957 (2022).
[7] J. Wang, K. Nagano, T. Shimada, and T. Kitamura, Strain-mediated multilevel ferroelectric random access memory operating through a magnetic field, RSC Adv. **4**, 45382 (2014).
[8] T. Xu, K. Switkowski, X. Chen, S. Liu, K. Koynov, H. Yu, H. Zhang, J. Wang, Y. Sheng, and W. Krolikowski, Three-dimensional nonlinear photonic crystal in ferroelectric barium calcium titanate, Nat. Photonics **12**, 591 (2018).
[9] V. A. Stoica, N. Laanait, C. Dai *et al.*, Optical creation of a supercrystal with three-dimensional nanoscale periodicity, Nat. Mater. **18**, 377 (2019).
[10] J. B. Tai and I. I. Smalyukh, Three-dimensional crystals of adaptive knots, Science **365**, 1449 (2019).
[11] Y. Zhang, Y. Sheng, S. Zhu, M. Xiao, and W. Krolikowski, Nonlinear photonic crystals: From 2D to 3D, Optica **8**, 372 (2021).
[12] M. Hadjimichael, Y. Li, E. Zatterin *et al.*, Metal–ferroelectric supercrystals with periodically curved metallic layers, Nat. Mat. **20**, 495 (2021).
[13] I. Chuang, R. Durrer, N. Turok, and B. Yurke, Cosmology in defect dynamics the laboratory: In liquid crystals, Science **251**, 1336 (1991).
[14] I. I. Naumov, L. Bellaiche, and H. Fu, Unusual phase transitions in ferroelectric nanodisks and nanorods, Nature (London) **432**, 737 (2004).
[15] A. Yadav, C. Nelson, S. Hsu *et al.*, Observation of polar vortices in oxide superlattices, Nature (London) **530**, 198 (2016).
[16] Z. Hong, A. R. Damodaran, F. Xue *et al.*, Stability of polar vortex lattice in ferroelectric superlattices, Nano Lett. **17**, 2246 (2017).
[17] N. Nagaosa and Y. Tokura, Topological properties and dynamics of magnetic skyrmions, Nat. Nanotechnol. **8**, 899 (2013).
[18] X. Z. Yu, W. Koshibae, Y. Tokunaga, K. Shibata, Y. Taguchi, N. Nagaosa, and Y. Tokura, Transformation between meron and skyrmion topological spin textures in a chiral magnet, Nature (London) **564**, 95 (2018).
[19] G. Posnjak, S. Čopar, and I. Muševič, Hidden topological constellations and polyvalent charges in chiral nematic droplets, Nat. Commun. **8**, 14594 (2017).
[20] N. Kanazawa, A. Kitaori, J. S. White, V. Ukleev, H. M. Ronnow, A. Tsukazaki, M. Ichikawa, M. Kawasaki, and Y. Tokura, Direct observation of the statics and dynamics of emergent magnetic monopoles in a chiral magnet, Phys. Rev. Lett. **125**, 137202 (2020).
[21] S. Das, Y. L. Tang, Z. Hong *et al.*, Observation of room-temperature polar skyrmions, Nature (London) **568**, 368 (2019).
[22] P. W. Forsbergh, Domain structures and phase transitions in barium titanate, Phys. Rev. **76**, 1187 (1949).

[23] D. Pierangeli, M. Ferraro, F. Di Mei, G. Di Domenico, C. E. M. de Oliveira, A. J. Agranat, and E. DelRe, Supercrystals in composite ferroelectrics, Nat. Commun. **7**, 10674 (2016).

[24] L. LoPresti, J. Parravicini, R. Soave *et al.*, Observation of an exotic lattice structure in the transparent $KTa_{1-x}Nb_xO_3$ perovskite supercrystal, Phys. Rev. B **102**, 214110 (2020).

[25] X. Zhang, Q. Yang, H. Liu, X. Wang, S. He, X. Li, and P. Wu, Switching effects of spontaneously formed superlattices in relaxor ferroelectrics, Opt. Mater. Express **9**, 4081 (2019).

[26] Q. Yang, X. Zhang, H. Liu, X. Wang, Y. Ren, S. He, X. Li, and P. Wu, Dynamic relaxation process of a 3D super crystal structure in a Cu:KTN crystal, Chin. Optic. Lett. **18**, 021901 (2020).

[27] L. Falsi, M. Aversa, F. Di Mei, D. Pierangeli, F. Xin, A. J. Agranat, and E. DelRe, Direct observation of fractal-dimensional percolation in the 3d cluster dynamics of a ferroelectric supercrystal, Phys. Rev. Lett. **126**, 037601 (2021).

[28] E. DelRe, E. Spinozzi, A. J. Agranat, and C. Conti, Scale-free optics and diffractionless waves in nanodisordered ferroelectrics, Nat. Photonics **5**, 39 (2011).

[29] E. DelRe, F. Di Mei, J. Parravicini, G. Parravicini, A. J. Agranat, and C. Conti, Subwavelength anti-diffracting beams propagating over more than 1 000 Rayleigh lengths, Nat. Photonics **9**, 228 (2015).

[30] F. Rosenberg, *Fundamentals of Crystal Growth I* (Springer-Verlag, Berlin, 1979).

[31] *Handbook of Crystal Growth*, 2nd ed., edited by T. Nishinaga (Elsevier, Amsterdam, 2015), Vol. 1.

[32] G. A. Samara, From ferroelectric to quantum paraelectric: $KTa1_{-x}Nb_xO_3$ (KTN), a model system, AIP Conf. Proc. **706**, 176 (2004).

[33] A. J. Agranat, C. E. M. de Oliveira, and G. Orr, Dielectric electro-optic gratings in potassium lithium tantalate niobate, J. Non-Cryst. Solids **353**, 4405 (2007).

[34] M. Ferraro, D. Pierangeli, M. Flammini, G. Di Domenico, L. Falsi, F. Di Mei, A. J. Agranat, and E. DelRe, Observation of polarization-maintaining light propagation in depoled compositionally disordered ferroelectrics, Opt. Lett. **42**, 3856 (2017).

[35] F. Di Mei, L. Falsi, M. Flammini, D. Pierangeli, P. Di Porto, A. J. Agranat, and E. DelRe, Giant broadband refraction in the visible in a ferroelectric perovskite, Nat. Photonics **12**, 734 (2018).

[36] L. Falsi, L. Tartara, F. Di Mei *et al.*, Constraint-free wavelength conversion supported by giant optical refraction in a 3D perovskite supercrystal, Commun. Mater. **1**, 76 (2020).

[37] L. Landau and E. Lifshits, On the theory of the dispersion of magnetic permeability in ferromagnetic bodies, Reprinted from Phys. Z. Sowjetunion **8**, 153 (1935).

[38] C. Kittel, Theory of the structure of ferromagnetic domains in films and small particles, Phys. Rev. **70**, 965 (1946).

[39] C. Kittel, Physical theory of ferromagnetic domains, Rev. Mod. Phys. **21**, 541 (1949).

[40] M. E. Lines and A. M. Glass, *Principles and Applications of Ferroelectrics and Related Materials* (Clarendon Press, Oxford, 1977).

[41] I. Muench, A. Renuka Balakrishna, and J. E. Huber, Periodic boundary conditions for the simulation of 3D domain patterns in tetragonal ferroelectric material, Arch. Appl. Mech. **89**, 955 (2019).

[42] A. Gumennik, Y. Kurzweil-Segev, and A. J. Agranat, Electrooptical effects in glass forming liquids of dipolar nano-clusters embedded in a paraelectric environment, Opt. Mater. Express **1**, 803 (2011).

[43] R. Pirc and Z. Kutnjak, Freezing in relaxor ferroelectrics and dipolar glasses, Phase Trans. **88**, 222 (2015).

[44] Z. Kutnjak and R. Pirc, Specific heat anomaly in relaxor ferroelectrics and dipolar glasses, J. Appl. Phys. **121**, 105107 (2017).

[45] C. E. M. de Oliveira, G. Orr, N. Axelrold, and A. J. Agranat, Controlled composition modulation in potassium lithium tantalate niobate crystals grown by off-centered TSSG method, J. Cryst. Growth **273**, 203 (2004).

[46] A. J. Agranat, R. Kaner, G. Perpelitsa, and Y. Garcia, Stable electro-optic striation grating produced by programmed periodic modulation of the growth temperature, Appl. Phys. Lett. **90**, 192902 (2007).

[47] A. Gordon and S. Dorfman, Kinetics of phase transitions in solid solutions of ferroelectric perovskites, Phys. Rev. B **51**, 9306 (1995).

[48] See Supplemental Material at http://link.aps.org/supplemental/10.1103/PhysRevLett.132.066603 for details on the setup, material, modeling, microscope images, and far-field temperature dynamics analysis.

[49] J. Pouget and G. A. Maugin, Solitons and electroacoustic interactions in ferroelectric crystals. I. Single solitons and domain walls, Phys. Rev. B **30**, 5306 (1984).

[50] A. W. Liehr, *Dissipative Solitons in Reaction Diffusion Systems* (Springer, Heidelberg, 2013), Chap. 3.

[51] F. Strocchi, *Symmetry Breaking*, Lect. Notes Phys. Vol. 732 (Springer, Berlin Heidelberg 2008).

[52] T. W. B. Kibble, Topology of cosmic domains and strings, J. Phys. A **9**, 1387 (1976).